

# Deep Learning-based Pipeline for Module Power Prediction from EL Measurements

Mathis Hoffmann<sup>\*1,3</sup>, Claudia Buerhop-Lutz<sup>\*2</sup>, Luca Reeb<sup>1,2</sup>, Tobias Pickel<sup>2</sup>, Thilo Winkler<sup>3,2</sup>, Bernd Doll<sup>2,3,4</sup>, Tobias Würfl<sup>1</sup>, Ian Marius Peters<sup>2</sup>, Christoph Brabec<sup>2,3,4</sup>, Andreas Maier<sup>1,4</sup>, and Vincent Christlein<sup>1</sup>

<sup>1</sup>Pattern Recognition Lab, Universität Erlangen-Nürnberg (FAU)

<sup>2</sup>Forschungszentrum Jülich GmbH, Helmholtz-Institute Erlangen-Nuremberg for Renewable Energies

<sup>3</sup>Institute Materials for Electronics and Energy Technology, FAU

<sup>4</sup>School of Advanced Optical Technologies, Erlangen

## Abstract

Automated inspection plays an important role in monitoring large-scale photovoltaic power plants. Commonly, electroluminescence measurements are used to identify various types of defects on solar modules, but have not been used to determine the power of a module. However, knowledge of the power at maximum power point is important as well, since drops in the power of a single module can affect the performance of an entire string. By now, this is commonly determined by measurements that require to disconnect or even dismount the module, rendering a regular inspection of individual modules infeasible. In this work, we bridge the gap between electroluminescence measurements and the power determination of a module. We compile a large dataset of 719 electroluminescence measurements of modules at various stages of degradation, especially cell cracks and fractures, and the corresponding power at maximum power point. Here, we focus on inactive regions and cracks as the predominant type of defect. We set up a baseline regression model to predict the power from electroluminescence measurements with a mean absolute error of  $9.0 \pm 8.4 W_P$  ( $4.0 \pm 3.7\%$ ). Then, we show that deep-learning can be used to train a model that performs significantly better ( $7.3 \pm 6.5 W_P$  or  $3.2 \pm 2.7\%$ ) and propose a variant of class activation maps to obtain the per cell power loss, as predicted by the model. With this work, we aim to open a new research topic. Therefore, we publicly release the dataset, the code and trained models to empower other researchers to compare against our results. Finally, we present a thorough evaluation of certain boundary conditions like the dataset size and an automated preprocessing pipeline for on-site measurements showing multiple modules at once.

---

\*equal contribution

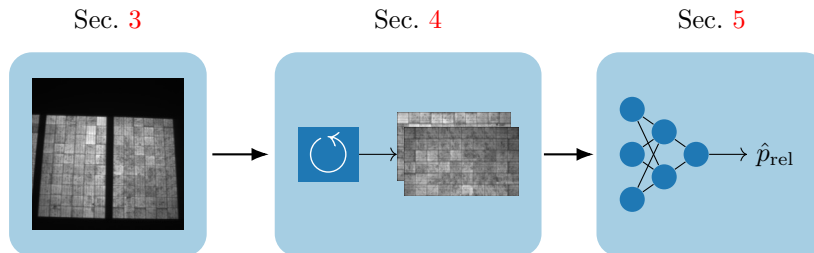


Figure 1: Overview of this work. First, data is collected on-site as well as under lab conditions. This is detailed in Sec. 3. Then, measurements are preprocessed to obtain a sequence of single modules, as described in Sec. 4. Here, preprocessing is denoted as  $\odot$ . Finally, power prediction is applied to obtain the estimated module power  $\hat{p}_{\text{rel}}$  relative to the nominal power  $P_{\text{nom}}$ . This is summarized by Sec. 5.

## 1 Introduction

Over the last years, photovoltaic (PV) power production has become an important factor in the energy production worldwide. This is promoted by decreasing module cost, increasing module power, long lifetime and low maintenance cost. More important, it produces power at a low ecological footprint and is hence used to fight global heating. However, continuous monitoring or regular inspections of PV power plants are necessary to ensure a constant and safe operation. In addition, modules might be damaged during manufacturing, transport, installation or operation and an early detection of those cases can help to avoid a later replacement at high cost.

It is common practice to operate multiple PV modules connected in series, commonly referred to as strings. As a result, a failure of a single module can drastically degrade the performance of the entire string. However, continuous monitoring is usually applied to strings and not to individual modules for economical reasons. To this end, manual inspection of single modules is required to further narrow down failures.

Lately, electroluminescence (EL) imaging is accepted as a useful tool by the community to analyze many failures of single modules, e.g., cell cracks and fractures. This is because many defect types can be identified easily and, as opposed to infrared (IR) measurements, a quantification of the active area of a cell is possible [5]. The latter makes it especially well suited for automated prediction of the module power by statistical methods like deep-learning (DL). Traditionally, the maximum power point (MPP) is determined from direct measurements of the IV curve. Although this is possible on-site, it requires to disconnect every single module to perform the measurement. Hence, this is time consuming and costly. In contrast, EL-based determination of the MPP enables an automated inspection of entire power plants, possibly also using unmanned aerial vehicles.

For PV-plant operators especially cell cracks and fractures with varying origin, including manufacturing process, transport, installation, operating conditions (e. g., storm, hailstorm, snow load) are of particular relevance. Note that, throughout this work, we refer to breaks of the cell that cause parts of it to become disconnected as fractures, whereas cracks are breaks that do not lead to disconnected regions. The impact of cell cracks on the module power and performance is studied intensely during the last years using EL-images for identifying cracks and IV-tracers for determining the module power [22, 20, 33, 30, 5, 14]. To study crack propagation, mostly climate chambers and static loading, e. g., using sand sacks, were used. Buerhop and Gabor studied the performance of modules during static and cyclic loading using a specialized setup [3, 15], where EL-measurements as well as power data were recorded at loaded and unloaded stages. In addition to the indoor experiments, Buerhop studied the performance of modules with cracked cells at an on-site test facility in detail [6]. All previous investigations have in common that two separate measurements are required: The EL-measurements are used to identify cracks and IV-tracing is used to determine the power at maximum power point (PMPP). Given that on-site IV measurements are costly, an automated and reliable estimation of the PMPP and the impact of cell cracks and fractures on the latter using EL-measurements are of particular importance for future studies. Note that, throughout this work, we use the terms module power and power at maximum power point interchangeably.

In a previous conference paper, we showed that the PMPP can be automatically predicted from EL measurements taken during indoor mechanical load testing experiments [8]. This work is a direct continuation and extension of that conference paper. As opposed to the previous work, we now focus on building regression models for on-site data. For efficiency reasons, on-site EL-measurements are usually conducted such that multiple modules are visible in a single measurement. Since we aim to predict the PMPP for single modules, we design a segmentation pipeline for on-site EL-measurements to automatically generate images showing only a single module. Furthermore, we add an extensive evaluation of the prediction performance, stability and boundary conditions. Finally, we automatically quantify the per cell power loss. The main contributions of this work are as follows:

- (1) We develop a method to predict the PMPP from a single on-site or indoor EL module measurement. We achieve a mean absolute error (MAE) of  $7.3 \pm 6.5 W_p$  and compare the result against alternative methods in a thorough evaluation. Since the dataset is specifically selected such that modules have a high shunt resistance, the trained models are restricted to this defect type.
- (2) We propose a fast and robust pipeline to detect and segment multiple modules in EL measurements, such that item (1) can be directly applied for on-site assessment of modules.
- (3) We perform an extensive evaluation of boundary conditions, such as mini-

mum image size and dataset size.

- (4) We set up and publicly release a dataset that is specifically compiled for the task at hand [7]. In addition, we publish our code and trained models\*, such that a direct application and comparison in future research is feasible and that our results directly scale to any other PV plant.
- (5) We predict the the per cell power loss and analyze the results in terms of defect severity. For our dataset that is compiled such that modules show a reduced active area in EL measurements, we find that the PMPP is dominated by fractures and that cracks are only of minor importance.

The remainder of this work is organized as shown in Fig. 1: In Sec. 3, we describe the data collection procedure and characterize the dataset used in this work. In Sec. 4, we describe the localization of multiple modules from single EL measurements. Then, in Sec. 5, we detail the automated power prediction. This includes baseline methods as well as DL-based methods.

Since the different parts of this work are of interest independent of each other, we decided to summarize the results of every part directly after describing the methodology and omit a detailed global results section. Then, we finally summarize the most important results in Sec. 6.

## 2 Related Work

In the last years, many efforts have been made to leverage computer vision methods in order to reduce the maintenance and operating cost of PV power plants. This includes automated defect analysis for solar cells [37, 25, 9] or automated prediction of solar irradiance [2]. In prior works, it has been shown that the number of cracks visible in EL measurements roughly correlates to the power loss of a module [12] and that the size of the inactive area on a module correlates well to the power of the module, as long as the overall fraction of inactive area remains small [35]. Furthermore, Karimi *et al.* have shown that the normalized power of the module can be determined from various features extracted from the EL image [21]. In addition, there are a few works on PMPP characterization using other methods as well. For example, Teubner *et al.* propose to use IR measurements of a module affected by potential induced degradation and compute the PMPP using linear regression from the mean temperature difference of the module to a reference module [38]. However, this procedure requires that the reference module is exposed to the same environmental conditions (air temperature, wind speed) as the module under test. This is especially challenging for roof-mounted PV installations, where the a temperature gradient is present due to the convective environment. Furthermore, the measurement accuracy is highly dependent on the available measurement time and steady environmental conditions. Recently, Ortega *et al.* proposed a continuous monitoring of PV power plants using measurement devices attached to every module [28]. Kropp *et al.*

---

\*<https://github.com/ma0ho/elpvpower>

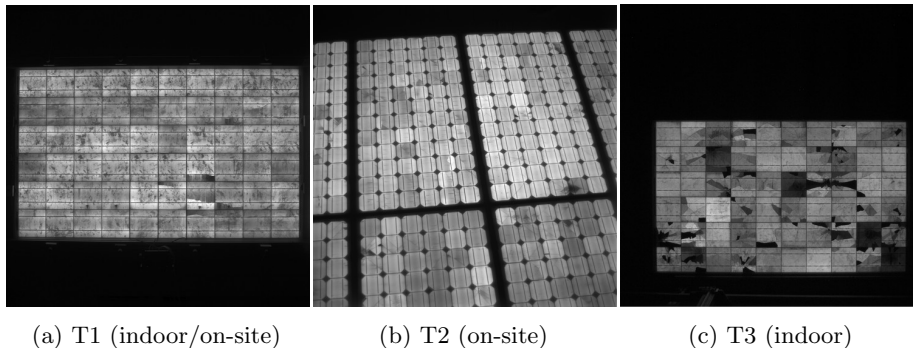


Figure 2: Example images from the data set.

manage to predict cell level characteristics from two EL measurements using simulations and finally calculate the module power for a single test module [23].

In contrast to the IR-based approach, our method does not require a reference temperature, since the magnitude of EL measurements mainly depends on camera characteristics and the excitation current, which is known in advance. Further, it is based on automated detection of defective areas rather than using module-wide statistics only. In contrast to the measurement-based approach by Ortega *et al.*, no additional hardware needs to be attached to the modules and the type and location of a defect can be determined additionally. As opposed to the simulation-based approach by Kropp *et al.*, our method only requires a single EL measurement of a module. In comparison to previous works on power estimation using a single EL measurement, our method does not rely on hand-crafted features. Instead, relevant features are learned from the data directly, resulting in a data-optimal regression model. Since no manual feature design is required, this method generalizes to various defect and module types, given an appropriate training dataset. Furthermore, it enables the visualization of the learned features and quantification of per cell or even per defect power losses, facilitating a better understanding for the roots of power degradation.

### 3 Data

We collected a large set of 719 EL measurements showing 137 module instances along with measurements of the maximum power point  $P_{\text{mpp}}$  at standard test conditions ( $1000 \text{ W m}^{-2}$ ,  $25^\circ$ ). The dataset is designed such that it has variations in the measurement procedure as well as in the type of solar modules. Overall, it contains three different module types, denoted as T1, T3 and T2 with nominal powers given by  $225 \text{ W}_P$  to  $235 \text{ W}_P$ ,  $235 \text{ W}_P$  to  $245 \text{ W}_P$  and  $170 \text{ W}_P$  to  $180 \text{ W}_P$  respectively. Furthermore, it also includes variations in the excitation currents, such that models trained using the data should be invariant to the excitation current to some degree. In particular, the excitation current for T3 is given by  $90\%_{ISC}$  (high current) and  $10\%_{ISC}$  (low current), whereas for T2 it is given by

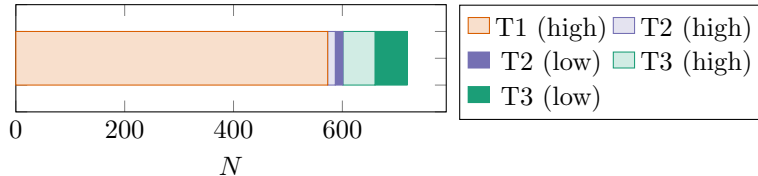


Figure 3: The dataset used in this work consists of three different module types (T1, T3, T2). Two of those have been measured at a high and low current, which indicated in brackets. Overall, the dataset consists of  $N = 719$  samples.

75% $_{ISC}$  (high current) and 50% $_{ISC}$  (low current). Finally it includes on-site measurements as well as measurements taken at controlled indoor conditions. Examples from the dataset are shown in Fig. 2. The distribution of samples between module types is shown in Fig. 3.

The EL measurements were recorded by a “Greateyes 2048 2048” silicon detector camera with 50 mm focal length lens and a camera triggered power supply. The camera parameters were fixed for the mechanical load testing site to an integration time of 5 s and an aperture of 2.4. They measurements have been recorded at 16-bit without image compression. Furthermore, the on-site measurements have been taken during night. Here, the integration time was also fixed to 5 s and the aperture was constant as well.

The PMPP of each PV module was determined from IV-curve measurements. For indoor measurements a table flasher “Spire Spi-Sun Simulator 4600 SLP” with estimated measurement uncertainty of 1.45% was used, while the indoor measurements at the mechanical load testing site have been carried out using a prototype of a permanent light source consisting of many halogen lamps. The results were extrapolated to standard test conditions (STC) with a measurement uncertainty of 3% to 4%. For on-site measurements, a “PVPM 1000CX” with a measurement uncertainty of at least 5% according to the data sheet, was used.

As seen from Fig. 3, the dataset is dominated by module type T1, because this type has been used for mechanical load testing [4]. During that procedure, load is simulated by an underpressure that is applied on the backside of each module. The underpressure is increased stepwise. After every increase, an EL and PMPP measurement is taken under load. Then, pressure is released and another set of measurements is taken, before a new load cycle is started. As a result, there are about 50 sets of measurements of a single module at different stages of loading including changes in the crack structures. Since these different stages of degradation come with a variance in PMPP, these load cycles are useful to assess, if a certain type of defect has an influence on the PMPP. Furthermore, as shown in Fig. 2, there is a series of on-site measurements using module type T1 as well.

The set of measurements using module type T2 only consists of on-site measurements. As opposed to T1, we vary the EL excitation current for this measurement series between high and low excitation. This is later used to

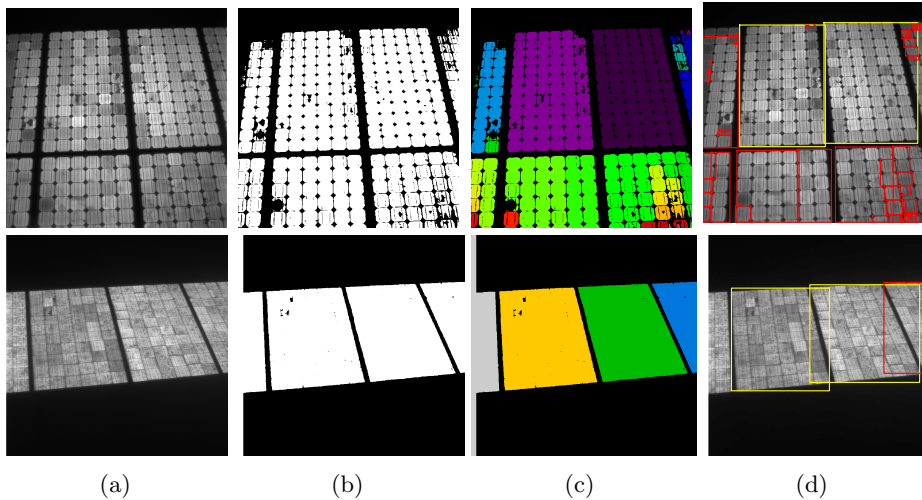


Figure 4: Preprocessing of multi-module measurements (top: module type T2, bottom: module type T3): Original image (Fig. 4a) is first downsampled and binarized (Fig. 4b). Next, connected component analysis is applied (Fig. 4c). Finally, bounding boxes of connected components are computed and implausible detections are rejected (Fig. 4d). Here, rejected detections are depicted by a red bounding box, whereas accepted detections are shown yellow.

obtain a model that performs well irrespective of the excitation current. The same holds for module type T3. This module type has been measured under indoor conditions again and includes variations in the excitation current, too. However, this type has not been subject to load testing experiments. Instead, the degradation is caused by natural events like hailstorms. An even more detailed analysis of the data can be found in Appendix C.

## 4 Localization of multiple modules

In this work, we use measurements from multiple sources. These include measurements taken under controlled lab conditions, as well as measurements taken on-site. For on-site measurements, it is common practice to capture multiple modules in a single image in order to reduce the overall number of measurements (cf. Fig. 2). In order to assess the power of a single module using these measurements, a localization of module instances is required. We propose a fast and straight-forward preprocessing pipeline to locate PV modules in EL measurements.

## 4.1 Preprocessing

During preprocessing, we make use of the fact that the background in EL measurements has a weak intensity, whereas the modules appear as densely connected regions with a high intensity. In addition, modules are usually clearly separated by a distinguished margin. Therefore, background and modules are easily separable by thresholding. We propose a five-step approach:

- (1) The original measurement is downscaled by  $s$ .
- (2) Binarization is performed using Otsu’s method [29]. As a result, the modules are clearly separated (cf. Fig. 4b).
- (3) Region candidates are computed by connected component labelling (cf. Fig. 4c) and subsequent region proposal (cf. Fig. 4d) [19].
- (4) Final module regions are obtained by rejecting implausible regions that do not adhere to simple constraints (cf. Fig. 4d and Sec. 4.2) and modules are segmented.
- (5) Perspective distortion of module images is removed using the method proposed by Hoffmann *et al.* [18].

The downscaling in item (1) is necessary, since the method is based on binarization and blob detection: Because we only aim at detecting entire modules, small structures such as cracks, busbars, cell borders or dirt are not of any interest to the detection at all. However, they regularly cause modules to appear as multiple separated blobs in the binarized images, which prevents the accurate detection of the modules. Fortunately, downscaling the images turned out as an efficient and simple method to counter these effects. At the same time, it speeds up subsequent computations.

## 4.2 Region constraints

The proposed pipeline results in a large number of false positives. This is due to noise in the background, parts of a module that are disconnected or modules that are only partially visible. The following constraints are applied to reject false positives:

- (1) Modules that are not completely visible in the measurement are not of interest in this work. Therefore, any detections that touch the boundary of a measurement are rejected.
- (2) Most of the outliers have a very small area, compared to the area of inliers. Therefore, any detections with an area small than  $\tau_s \cdot a_{\max}$  are rejected. Here,  $a_{\max}$  refers to the area of the largest detection in a measurement and  $\tau_s$  is a hyperparameter.

As a result, we obtain a method that has only two hyperparameters: The scale  $s$ , at which measurements are processed and the minimum area relative to the maximum area  $\tau_s$ .



### 4.3 Experiments

The hyperparameters of this method require proper tuning. To this end, we set up a separate dataset using a total of 37 measurements from the original on-site measurements. In summary, these measurements show two to seven completely visible modules each. We manually annotate bounding boxes for every completely visible module. Finally, we split the dataset into 25 training measurements with 75 completely visible modules and 12 test measurements with 31 modules.

For hyperparameter tuning, we use the Optuna library v1.2 [1] with default settings. Since we are mostly interested in a high detection rate and low false positives, we resort to maximizing the  $F_1$  score. Here, the  $F_1$  score is defined as the harmonic mean of precision and recall. Hence, it jointly accounts for the number of false positive and false negative detections. In order to compute the  $F_1$  score for a set of detected and ground truth object boxes, it is necessary to assess, if a ground truth box has been detected and, vice versa, if a detection corresponds to a ground truth box or is a false positive. To this end, we state that a module is detected, if the intersection over union (IoU) between detected and ground truth bounding box is at least  $\tau_{\text{IoU}} = 0.9$ . Here, the IoU is defined as the size of the intersection area divided by the size of the union area between two bounding boxes. Hence, the IoU is maximized, if two bounding boxes overlap perfectly. Then, we calculate the  $F_1$  score and perform the optimization on the training set. Overall, the problem is optimized using 30 trials with the default tree-structured Parzen window trial generator. We find that  $s = 0.23$  and  $\tau_s = 0.42$  gives the best results on our training split with an  $F_1$  score of 1.

### 4.4 Results

The detection performance on the test split evaluates as  $F_1 = 0.94$  using the same threshold  $\tau_{\text{IoU}} = 0.9$ . Detailed results on the detection performance using different thresholds can be found in Appendix A. We find that the method performs very well for  $\tau_{\text{IoU}} < 0.9$  and performs slightly worse for larger values of  $\tau_{\text{IoU}}$ . However, given that we are mostly interested in a high detection rate rather than very accurate detections, the performance is very good. Further, the method only takes about 322 ms (i7-8650U CPU) for a single image. Please also note that this method does not make any assumptions on the number of modules visible in a single image. Hence,  $s$  is estimated independent of the number of modules, although the optimal scale is dependent on the number of modules or the resolution of a single module.

## 5 Power prediction

We estimate the power  $P_{\text{mpp}}$  at the maximum power point (STC conditions) of a module using a single EL image and the nominal power according to the data sheet  $P_{\text{nom}}$  of the latter. We set up a baseline using support vector regression (SVR) in Sec. 5.2. We describe our DL-based approach in Sec. 5.3. In

order to make the results using SVR and DL comparable, we stick to a common experimental procedure, which we describe in Sec. 5.1. Finally, in Sec. 5.4, we compare both approaches and report experimental results.

Throughout this work, we assume that the nominal power  $P_{\text{nom}}$  is known for every module. Then, we estimate the power relative to  $P_{\text{nom}}$ , i. e.,

$$P_{\text{mpp}} = p_{\text{rel}} \cdot P_{\text{nom}} \quad (1)$$

and denote estimates of the relative power  $p_{\text{rel}}$  by  $\hat{p}_{\text{rel}}$ . Note that, for this dataset,  $p_{\text{rel}}$  roughly correlates to the amount of the inactive area of a module ( $r = 0.90$ ). While we cannot say, if the slope of a linear model predicting  $p_{\text{rel}}$  from the amount of inactive area is the same for every module type, we expect that the observed correlation between the two quantities holds for other module types as well. This is also supported by the work of Schneller *et al.* that comes to a similar observation using different data [35].

## 5.1 Evaluation protocol

The overall goal is to find a model that predicts  $p_{\text{rel}}$  with a low average error and a small number of outliers. For evaluation purposes, we report the MAE over all samples, as well as the root mean squared error (RMSE). The MAE is given by

$$= \frac{1}{N} \sum_{i=1}^N |p_{\text{rel}}^{(i)} - \hat{p}_{\text{rel}}^{(i)}| \quad (2)$$

while the RMSE is computed as

$$= \frac{1}{N} \sqrt{\sum_{i=1}^N (p_{\text{rel}}^{(i)} - \hat{p}_{\text{rel}}^{(i)})^2} . \quad (3)$$

Since the dataset is relatively small, making statistically significant statements on model performance using a conventional train/test split of the dataset is hard, since results are necessarily computed on a relatively small test set. To overcome this limitation, we conduct a cross validation (CV), such that the complete dataset is used for testing. We initially split the dataset into 5 folds using stratified sampling, such that the overall distribution of relative powers is preserved between folds. Since a stratified sample requires distinct class labels, we discretize  $p_{\text{rel}}$  in 20 distinct bins, where each bin has a range of 5%. Further, we make sure that none of the solar module instances ends up in two different folds.

The baseline method as well as the DL-based methods have hyperparameters that need to be tuned properly. In order to enable a fair comparison between methods, we establish a standard protocol. We perform the hyperparameter optimization using Optuna library v1.2 [1] with the default settings and 250 iterations in every fold of the CV to make sure that no test data is used for hyperparameter optimization. Then, we split the training folds into a training

and a validation set. While the first one is used to determine model parameters, the latter one is used to optimize hyperparameters. We empirically found that the validation set needs to be large enough to obtain stable results. To this end, we use 40% of the training data for validation. Again, we perform a stratified split, such that the label-distributions are similar in training and validation set.

## 5.2 Baseline

In this section, we propose a baseline approach to estimate the  $P_{\text{mpp}}$  from a single EL image. We train the SVR using features extracted from the EL measurements.

### 5.2.1 Feature extraction

To apply power estimation using the SVR, we map the data to a low dimensional feature representation. This representation is defined such that as much as possible information that is required to estimate the power, is preserved. In previous works, Zernike moments and Wavelet features have been successfully applied to recognize textured defects such as cracks on PV modules [24, 13]. However, we know that the power of a module is largely dominated by fractures, since our dataset is carefully compiled to adhere to this property. Since fractures are mainly blob-like defects, we use the measurement mean and standard deviation, which is a good representation for that. Furthermore, it has been shown that features extracted from models pretrained on the ImageNet [10] dataset are useful for machine learning tasks on different data as well [26, 36]. Therefore, we include features extracted from a pretrained ResNet18 as well [16]. The ResNet architecture has become popular for many computer vision problems. It is available in different configurations featuring between 18 and 152 layers. It was the first architecture that introduced residual connections between subsequent layers, which mainly solved the issue of vanishing gradients. As a result, it enables to increase the number of layers of a DL architecture. To compute the ResNet18-features  $f_{\text{R18}}$ , we convert measurements into RGB images and perform channel-wise normalization using the per-channel statistics. Hence, we make sure that the statistics of the measurements match those of the ImageNet [10] dataset that has been used during training. For the pretrained ResNet18, we use the model available in the open-source DL framework PyTorch v1.3 [31] and drop the fully connected layer to obtain features directly after global average pooling. On the other hand, the features composed of the mean and standard deviation of intensities  $f_{\mu,\sigma}$  is computed without further preprocessing.

The feature extraction is followed by a normalization. Here, we compute the mean and standard deviation of every feature independently using all samples from the training data. We use these statistics to normalize training, as well as test features.

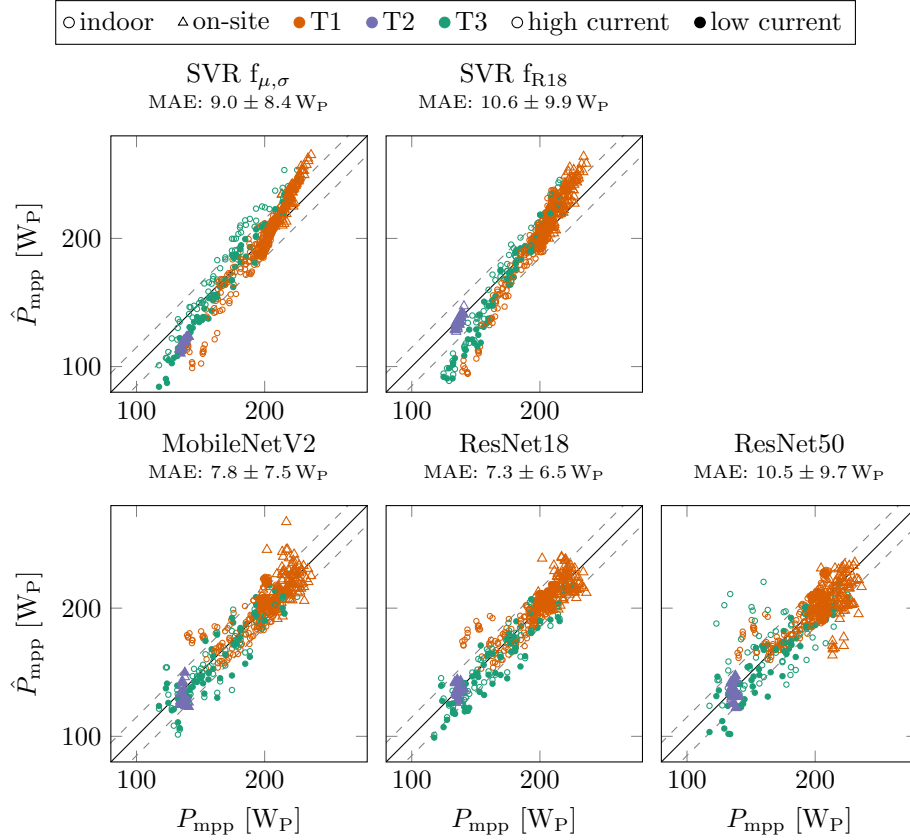


Figure 5: Distribution of estimation errors of all methods. We aggregate the results from all folds of the cross validation (CV), such that all samples of the dataset are shown here. For the samples, we distinguish between indoor  $\circ$  and on-site  $\triangle$  measurements by marker shape. Further, we distinguish between module type T1  $\bullet$ , T2  $\bullet$  and T3  $\bullet$  by marker color. Finally, we differentiate measurements taken at high current  $\circ$  or low current  $\bullet$  by marker filledness. For better visualization, the ideal regression line is shown  $\text{---}$ . Furthermore,  $\text{---}$  indicates the  $0 \pm 15 W_P$  isoline.

### 5.2.2 Experimental procedure

The SVR regression aims to minimize the absolute regression error

$$|\Delta p_{\text{rel}}| = |p_{\text{rel}} - \hat{p}_{\text{rel}}| \quad (4)$$

for those samples that have  $\Delta p_{\text{rel}} > \epsilon$ , while maintaining a regression model with a small Lipschitz constant. Here,  $\epsilon$  is the width of the epsilon-tube within which errors do not contribute to the loss of the SVR objective function [11]. We use the implementation from the Scikit-learn library v0.20 [32] with the default radial basis function kernel. For the width of the epsilon-tube and the regularization constant, we conduct a hyperparameter optimization in every fold as described in Sec. 5.1.

## 5.3 Deep-learning

In this section, we introduce the DL-based approach to predict  $P_{\text{mpp}}$  given an EL-measurement as well as the nominal power  $P_{\text{nom}}$  of the module. We present a straightforward approach and use standard DL-architectures that have been trained on ImageNet [10] to perform regression of  $\hat{p}_{\text{rel}}$  (see Eq. (1)). We detail our methodology in Sec. 5.3.1 and focus on the pipeline that empirically worked best. In Sec. 5.3.2 we explain, how we tuned the hyperparameters for different DL-models.

### 5.3.1 Method

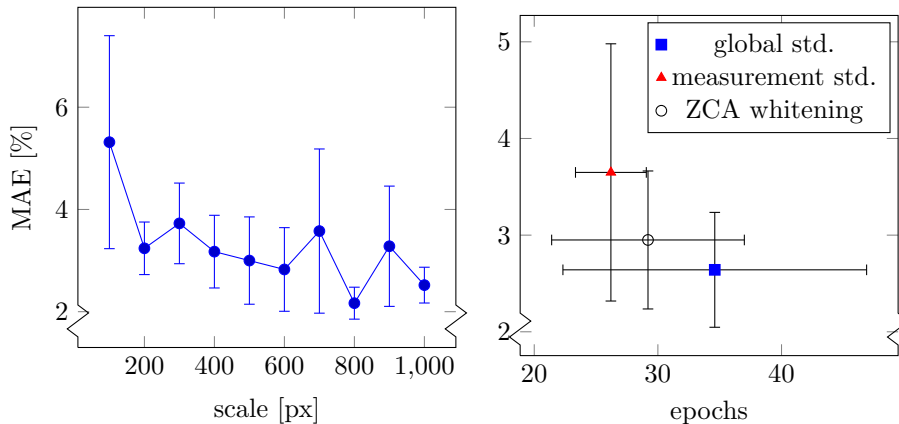
As deep neural networks (DNNs) are usually trained end-to-end, meaning that the feature extraction is part of the training process, there are only a few design choices that need to be made. These include (1) the preprocessing that is applied to the raw measurements (2) the DL-models that are used (3) the loss function (4) the optimization method. We detail our choices in the next paragraphs:

**Preprocessing** Although we only use fully-convolutional networks, it is common to limit the resolution of input measurements to reduce the computational effort. We rescale measurements such that the smallest side equals 800 px. Then, we normalize the measurements using the common normalization with global statistics. To this end, we compute the mean  $\mu$  and standard deviation  $\sigma$  of photon counts using our data. A sample  $x$  is then normalized according to

$$x' = \frac{x - \mu}{\sigma}. \quad (5)$$

The choices of scale and normalization scheme are verified by initial experiments reported in Fig. 6.

Furthermore, we apply online data augmentation during training. As already reported by Deitsch *et al.* [9] for the case of single cells, light data augmentation is sufficient, since the segmented modules are mostly fixed in orientation and position due to the module detection and removal of perspective distortion.



(a) Sensitivity of the error with respect to variations in measurement scale. (b) Sensitivity of the error with respect to variations in the normalization scheme.

Figure 6: We conduct a series of initial experiments to determine the best measurement scale and normalization scheme. All experiments were performed using ResNet18 without further hyperparameter tuning. Every model is trained 5 times until convergence. We report the minimum MAE on the validation set. Error bars denote the standard deviation of the MAE between training runs. In Sec. 5.3.1, we scale the smallest side of the measurement to the specified value. In Sec. 5.3.1, we compare the common global normalization, where all measurements are normalized by the same statistics computed over the whole training set to a measurement-wise approach, where every measurement is normalized using its own statistics. Finally, we include normalization by patch-wise zero component analysis (ZCA)-whitening. It turns out that a scale of 800 px and the common global normalization give the best results.

We apply random horizontal and vertical flips, random rotation by at most  $\pm 10^\circ$ , random translation by 5% of the image size at maximum and random downscaling to 80% of the image size at minimum. The augmented images are zero-padded to match the original image size.

**DL models** In many recent works, it has been shown that applying transfer learning is advantageous over training models from scratch, even if source and target domain differ [39]. Therefore, we resort to using standard architectures, where pretrained weights are readily available. In this work, we focus on three different architectures: First, we include a small and a larger network from the ResNet architecture family (ResNet18 and ResNet50) [16]. This allows us to investigate, if deeper architectures are beneficial for the task at hand. In addition, we include the MobileNetV2 architecture [34], which is specifically designed for high throughputs at inference time, since this is a major benefit for

practical applications.

For every one of those models, the final layer is composed by a matrix multiplication that maps the high dimensional feature representation to the correct output size. This layer is often referred to as the fully connected (FC) layer. We replace the final FC layer by a randomly initialized FC layer with a single output. We do not perform any non-linear activation on the output. Hence, this corresponds to a linear regression of  $p_{\text{rel}}$  using the features from previous layers.

**Loss function** Common loss functions for regression problems include the mean squared error (MSE) and MAE. By definition, MSE puts a higher weight on outliers, resulting in a model that performs better for underrepresented cases and worse for overrepresented cases. Since we are interested in a model that performs well over a large range of samples, we minimize the MSE.

**Optimization** A huge variety of optimization methods has been proposed in the literature. For this work, we decided to use some of the most prevalent approaches: We use stochastic gradient descent (SGD) with momentum  $\nu = 0.9$  and weight decay  $\lambda$  and properly tune the learning rate  $\eta$ , batch size  $B$  and weight decay  $\lambda$  independently for every architecture. For the learning rate schedule, we reduce the learning rate as soon as the validation loss does not decrease for 20 epochs. Here, an epoch refers to training once on the complete training dataset.

### 5.3.2 Experimental procedure

Proper tuning of hyperparameters is crucial in order to perform a fair comparison of different architectures. We use the Optuna library v1.2 [1] to determine the optimal values for  $\eta$ ,  $B$  and  $\lambda$  individually for every architecture and fold of the CV, as described in Sec. 5.1. The results are summarized by Tab. 1. We find that optimal parameters are relatively similar across architectures.

As soon as the optimal hyperparameters are determined, we use them to train a final model for every fold that is then tested using the test data of the respective fold. As opposed to the hyperparameter search, we now use 80 % of the data for training and only 20 % for validation. We further apply early stopping after 40 epochs without improvement on the validation set and use the checkpoint that performed best on the validation set for testing.

## 5.4 Results

In this section, we assess the performance of the architectures for the prediction of PMPP and compare it to the performance of the baseline model. By training 5 CV folds with every architecture using the parameters found by hyperparameter optimization, we assess the stability of every method with respect to variations in the training and test data. We report the results on the test folds in Fig. 7 and in Tab. 2. It turns out that ResNet18 and MobileNetV2 have a smaller

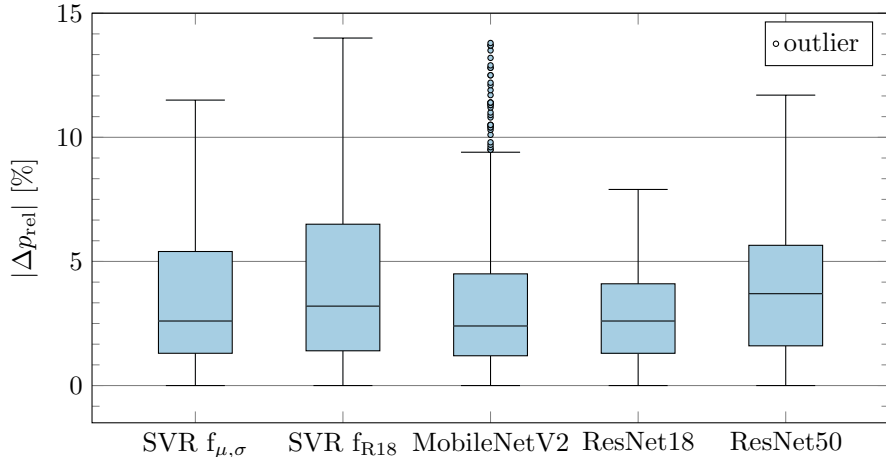


Figure 7: Distributions of sample errors over all 5 folds of the CV. The errors are computed on the testset of every fold. Note that the  $y$  axis has been cut at  $|\Delta p_{\text{rel}}| = 15\%$  for better visualization.

average MAE than the baseline, whereas ResNet50 does not perform well. This is explained by the relatively small dataset. Among the SVR-based methods,  $f_{\mu,\sigma}$  has the lowest MAE. However, it also shows the strongest variation between folds, indicating that the result is very data dependent. Overall, ResNet18 gives the lowest MAE and RMSE.

In terms of variation between CV folds, ResNet50 turns out most stable. However, the advantage over ResNet18 is neglectible. We observe that the gap between MAE and RMSE is smaller for the DL-based models compared to the SVR-based ones. This is explained by the difference in the loss function, since SVR roughly minimizes the MAE (cf. Eq. (4)), whereas we chose to minimize the MSE for the DL-based models.

In Fig. 5, we show the distribution of errors for all samples in the dataset and all methods. This is obtained by merging all five test folds into a single figure. The comparison shows that the predictions of ResNet18 are well aligned with the ideal regression line, whereas the predictions using SVR are skewed with respect to the ideal line. We conclude that this is caused by the features chosen for the regression model that do not result in a linear regression problem under the RBF kernel. However, initial experiments with other kernels performed even worse. We also compute the  $p$ -value using a  $t$ -test to assess, if the ResNet18 performs significantly better than the other approaches. We find that the performance difference to the MobileNetV2 is not statistically significant, whereas ResNet18 performs significantly better than the remaining other methods ( $p < 0.0001$ ).

Finally, in Tab. 3, we summarize the results for different subsets of the data. It turns out that the prediction is stable across most of the different subsets. The only exception are those modules measured at a low excitation current and



	$B$	$\lambda$	$\eta$
MobileNetV2	8	$1.00 \pm 1.01 \times 10^{-2}$	$3.54 \pm 11.30 \times 10^{-3}$
ResNet18	8	$2.59 \pm 0.69 \times 10^{-2}$	$3.41 \pm 5.70 \times 10^{-3}$
ResNet50	8	$1.79 \pm 2.44 \times 10^{-2}$	$3.38 \pm 8.80 \times 10^{-3}$

Table 1: Results from the hyperparameter optimization using Optuna library v1.2 [1]. The hyperparameter optimization has been performed using 250 iterations per model. We optimize the the batch size sampling from  $B \in [8, 16, 32, 64]$ , the learning rate sampling from  $\eta \in [1 \times 10^{-5}, 1 \times 10^{-1}]$  and the weight decay sampling from  $\lambda \in [1 \times 10^{-3}, 1 \times 10^{-1}]$  in logspace. Sampling is performed using the default tree-structured Parzen window approach and unsuccessful trials are pruned.

	MAE [%]	RMSE [%]	MAE [W <sub>P</sub> ]	RMSE [W <sub>P</sub> ]
MobileNetV2	$3.4 \pm 3.2$	4.7	$7.8 \pm 7.5$	4.7
ResNet18	$3.2 \pm 2.7$	4.2	$7.3 \pm 6.5$	4.2
ResNet50	$4.5 \pm 4.1$	6.2	$10.5 \pm 9.7$	6.2
SVR $f_{\mu,\sigma}$	$4.0 \pm 3.7$	5.5	$9.0 \pm 8.4$	5.5
SVR $f_{R18}$	$4.6 \pm 4.2$	6.2	$10.6 \pm 9.9$	6.2

Table 2: Quantitative results computed by CV. We show the MAE and the RMSE averaged over the test sets of every fold of the CV. In addition, the standard deviation of errors is shown. Finally, we explicitly show the relative error, as used in training as well as the absolute error in [W<sub>P</sub>] for better interpretability.

modules of type T3. Both of them perform worse than the others. Subset T3 is composed of modules measured at high and low current. Hence, it contains the same modules twice. We find that modules from subset T3 that are measured at high current result in a MAE of 4.3%, whereas modules from the same subset measured at a low current result in a MAE of 4.7%. Specifically, modules from subset T3 are mostly underestimated and we find that this effect is more severe for modules measured at a low current. Since those results have been computed using the same module instances and are averaged over all 5 folds of the CV, we can conclude that the model performs slightly better on measurements taken at a high current, irrespective of the module type. However, this result might be biased by the fact that the dataset is largely dominated by samples measured at a high current.

#### 5.4.1 Visualization of Class Activation Maps

In previous works, it has been shown that object locations can be extracted from DNNs trained for object classification [27]. To this end, the activation maps from the last layer that preserves spatial information are used to calculate a

	MAE [%]	RMSE [%]	MAE [W <sub>P</sub> ]	RMSE [W <sub>P</sub> ]	<i>N</i>
indoor	3.1 ± 2.8	4.1	7.1 ± 6.6	9.7	596
on-site	3.6 ± 2.7	4.5	8.1 ± 6.2	10.1	123
high current	3.0 ± 2.7	4.0	6.9 ± 6.2	9.3	646
low current	4.5 ± 3.3	5.5	10.3 ± 8.0	13.0	73
T1	2.7 ± 2.6	3.7	6.2 ± 6.0	8.6	478
T2	2.6 ± 1.8	3.1	4.5 ± 3.2	5.5	28
T3	4.6 ± 3.1	5.5	11.0 ± 7.5	13.3	118

Table 3: Results on different subsets of the data using ResNet18. We compute the mean absolute error (MAE) and the root mean squared error (RMSE) using the test samples from all 5 folds. In addition, the standard deviation of errors between folds is shown as well as the number of samples *N*.

heatmap of possible object locations. This concept is now widely known as class activation map (CAM). In a recent work, we used this to segment cracks in EL measurements using a ResNet18 [25].

We propose to build upon this work and use a slightly modified ResNet18 that allows one to infer the predicted power loss for an arbitrary area by integrating over the respective area of the CAM. The ResNet18 is constructed such that it computes 512 feature maps given an input image. However, we are interested in a single feature maps that gives the power loss per pixel. To this end, we append a  $1 \times 1$  convolution using a single kernel to reduce the number of feature maps to a single map *f*. Since we want every pixel of *f* to quantify the loss of relative power of the corresponding area of the measurement, we need to constrain the resulting map such that it is strictly negative. This is achieved by appending a ReLU, followed by a Sign layer. Here, the ReLU refers to a function that is the identity for input values greater zero and zero otherwise, whereas the Sign layer flips the sign of the input. The resulting feature map  $f_{\text{cam}}$  is later used for further assessment. Since  $f_{\text{cam}}$  gives the per-pixel power loss, the total power loss is computed by summing over  $f_{\text{cam}}$ . Hence, instead of computing  $\hat{p}_{\text{rel}}$  directly from the activations after global average pooling (GAP) using a fully connected layer, we now compute  $\hat{p}_{\text{rel}}$  as

$$\hat{p}_{\text{rel}} = 1 + \sum_{i,j \in \Omega_f} \underbrace{-\text{ReLU}(f_{i,j})}_{f_{\text{cam}}}. \quad (6)$$

Since this only consists of operators that are sub-differentiable w. r. t. the inputs, we can readily implement this using PyTorch v1.3 [31] and train it end to end. As opposed to regular CAMs that are computed using unconstrained activation maps, the proposed formulation assures that the activations are in a physically plausible range and hence, a direct interpretation as physical quantities is possible.

Our experiments showed that for successful training, a scaling of *f* by  $|\Omega_f|$  is necessary to counter an exploding MSE loss. Further, we note that  $f_{\text{cam}}$  contains

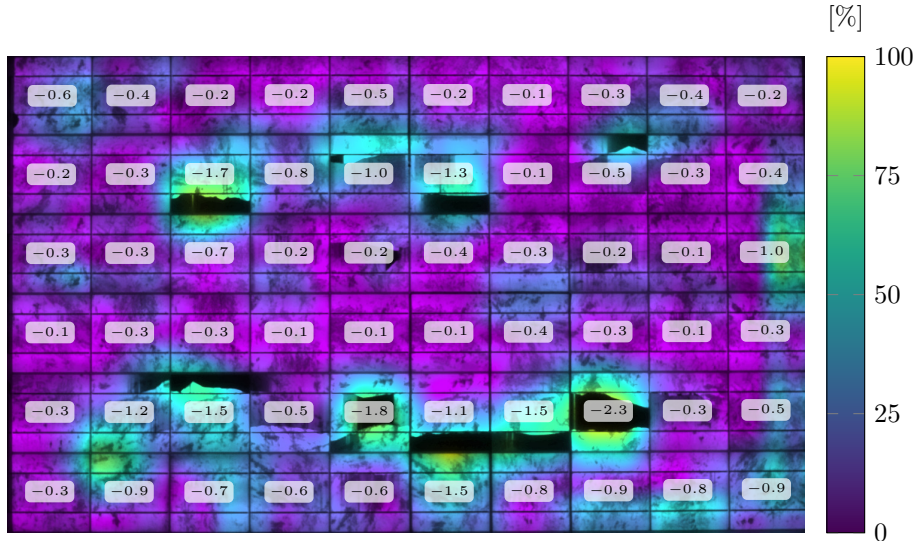


Figure 8: Visualization of class activation map (CAM) using a modified ResNet18. Note that we color-code the original EL measurement with the given colormap using the relative magnitude of  $-f_{\text{cam}}$  such that brighter colors correspond to regions with high relative power loss. Since the intensity is given by the original measurement, color appearance does not exactly correspond to the legend, since the legend uses a linear intensity ramp. For every cell, we give the power loss determined by the model in  $W_p$ . This is computed by integrating over the corresponding area of the CAM, resulting in the relative power loss, which is converted into the absolute power loss by Eq. (1).

a small constant bias after training. We remove that bias by subtracting the median of multiple  $f_{\text{cam}}$  computed from module images with  $p_{\text{rel}} \approx 1$  from all  $f_{\text{cam}}$ .

The results are shown in Fig. 8 and additional examples can be found in Appendix B. It turns out that the resulting CAMs mostly highlight the fractures, indicating that the network is able to learn physically relevant features and that fractures are the main source of power loss as opposed to cracks.

It becomes apparent that, in many examples, the amount of power loss per cell predicted by the network is roughly proportional to the amount of inactive area. Although this might appear obvious at first, this is not a trivial finding, because there are various types of cracks and their relative position is important as well. For example, it is known that the current and with the the power of a string is limited by the worst cell, since all cells are connected in series. However, at least for this dataset, the network reveals a linear relationship between the amount of inactive area and module power. To verify this, we compute the size of inactive area for every module in the dataset by thresholding and calculate the power loss proportional to the inactive area, which is similar to the thresholding

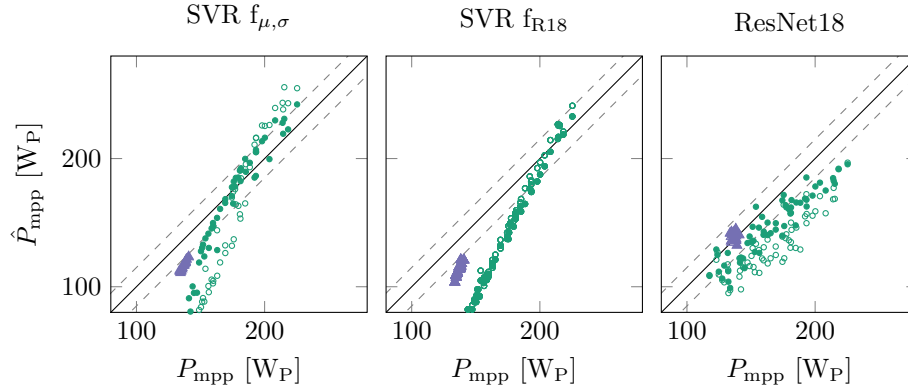


Figure 9: Distribution of estimation errors for the generalization experiment. For the samples, we distinguish between indoor  $\circ$  and on-site  $\blacktriangle$  measurements by marker shape. Further, we distinguish between module type T2  $\bullet$  and T3  $\blacktriangle$  by marker color. Finally, we differentiate measurements taken at high current  $\circ$  or low current  $\bullet$  by marker filledness. For better visualization, the ideal regression line is shown  $\text{—}$ . Furthermore,  $\text{---}$  indicates the  $0 \pm 15 W_P$  isoleine.

	MAE [%]	RMSE [%]	MAE [ $W_P$ ]	RMSE [ $W_P$ ]
ResNet18	$9.5 \pm 6.0$	11.3	$22.6 \pm 14.8$	27.0
SVR $f_{\mu, \sigma}$	$14.8 \pm 11.4$	18.6	$34.0 \pm 27.9$	43.9
SVR $f_{R18}$	$17.1 \pm 10.0$	19.8	$39.3 \pm 24.8$	46.4

Table 4: Quantitative results of the generalization experiment. We show the MAE and the RMSE as well as the standard deviation of errors. Finally, we explicitly show the relative error, as used in training as well as the absolute error in [ $W_P$ ] for better interpretability.

approach by Schneller *et al.* [35]. Using this approach, the module power is predicted with a MAE of  $8.5 \pm 2.1 W_P$ , which is on par with the baseline results reported in Fig. 7. It is possible that those results could be improved even further by using more than a single threshold, because this would allow the model to take variations in the shunt resistance into account.

## 5.5 Generalization to unseen Data

Finally, we aim to assess, if the method generalizes well to module types that have not been used during training. This experiment is conducted using the ResNet18, since this performed best in the previous experiments. In addition, we include the SVR-based methods for reference. We train the model on samples T1 using the hyperparameters that have been found in the first fold of the CV and test on samples T2 and T3. Note that the module types differ in their physical

properties. For example, T1 and T3 consist of  $10 \times 6$  polycrystalline cells, of which each has an edge length of 6 inch, whereas T2 consists of  $12 \times 6$  cells with an edge length of 5-inch. Furthermore, they also differ in their nominal power, which is given as  $230 W_P$  for T1,  $170 W_P$  for T2 and  $240 W_P$  for T3. However, all types have in common that their cells are arranged in 3 substrings that are connected in parallel and include a bypass diode for every substring.

The results are summarized by Fig. 9 and Tab. 4. It turns out that the performance degrades in this setting. For example, the performance of ResNet18 is lowered to  $9.5 \pm 6.0\%$  (as opposed to  $3.2 \pm 2.7\%$  when training on the whole dataset), while the performance drop for the SVR-based methods is even larger.

From Fig. 9, it becomes apparent that, especially the ResNet18 generalizes well to T2, although it has never been trained on monocrystalline modules. However, it does not generalize well to T3. This result is in line with the results reported in Tab. 3, where it turns out that the model trained on all subsets performs worst on T3 as well.

We conclude that the dataset bias, which is already observed in Appendix C, limits the generalization ability of the method to unseen module types. This problem could most likely be solved by using a larger dataset that covers a greater variety of module types.

## 6 Conclusion and Future Work

In this work, we propose a novel method to assess the power of individual PV modules using a single electroluminescence measurement only. We combine classical image processing methods for segmentation of multiple modules with a deep-learning-based prediction of the power at maximum power point. We find that our method is capable to predict the power at maximum power point with an average MAE of  $7.3 \pm 6.5 W_P$  in a cross validation. This is already close to the measurement error of the system, which is specified as 2% (indoor) and 5% (on-site), resulting in a lower bound to the MAE of  $4.6 W_P / 11.5 W_P$ . Although the choice of a ResNet18 and the reported hyperparameters are specific to the dataset used in this work, we are confident that they hold for other datasets as well, since previous experiments on defect recognition lead to similar conclusions [25].

For this work, we use a dataset of 719 EL measurements including three module types. However, we experimentally show that the model does not generalize well to unseen module types. This cannot be solved by data augmentation, since this is most likely caused by differing module properties like busbar configurations. We are confident, that the generalization can be improved by training on a larger dataset comprising more different types of modules. This is because a greater variety in the training data would help the model to learn the most important features for power prediction, rather than overfitting on certain defect types that only occur for a specific module type. We point out that the dataset is selected such that the modules have a high shunt resistance. Other defect types like potential induced degradation are not taken into consideration. As a result,

the trained models are restricted to this particular type of defects. However, we are confident that the method can be applied to other defect types as well, as long as they are visible in EL measurements and a comprehensive training dataset is available.

We transfer the concept of class activation maps to the regression task and use it to calculate the power loss per cell jointly with the power loss of the overall module. Since the per cell power loss has never been used during training, this approach allows to quantify the impact of individual defects on the overall power output and does not require any additional measurements or finite element analysis. Our experiments show that the model can automatically determine the defect types that are most relevant to calculate the power loss of the module. By means of the thresholding experiment, we show that this quantification of power losses can help to design simpler methods that only perform slightly worse, compared to the DL-based approach.

Furthermore, we compile and release the dataset consisting of 719 EL measurements that have been acquired under varying conditions as well as measurements of the  $P_{\text{mpp}}$  at standard test conditions. This includes indoor and on-site measurements as well as measurements from load cycle experiments. As some of the on-site measurements show multiple modules at the same time, we propose a simple yet robust preprocessing pipeline to detect and segment module instances. We evaluate the detection of modules on a separate testset and find that it results in a detection rate of  $F_1 = 0.94$ . This detection pipeline is currently designed to detect modules that do not have a defective substring. Modules with a defective substring result in two separate detections, since the parts are not connected in the binarized measurement. An extension of the method for such cases is subject to future works.

For future works, we think that it might be interesting to consider architectures that operate on cell level, because they could take the electrical connections into account, which is not considered in this work. As shown in Sec. 5.4.1, the model mainly focusses on fractures, which is consistent to physical considerations and prior works. However, the impact of a fracture on the PMPP is dependent on the overall conductivity of the substring. This relationship could be learned from the data using an architecture that determines the fraction of inactive area per cell and subsequently combines this information into a final estimate. Further, the generalization gap shown in Fig. 9 deserves further investigation.

We are confident that this work contributes to an automated and contactless assessment of large PV power plants. By releasing the data and code, we aim to allow other researchers to reproduce our results and to push the field forward.

## Acknowledgements

We gratefully acknowledge the BMWi as well as the IBC SOLAR AG for financial funding of the project iPV4.0 (FKZ: 0324286) and the German Federal Ministry for Economic Affairs and Energy (BMWi) for financial funding of the project COSIMA (FKZ: 032429A). Furthermore, we acknowledge the PV-Tera grant by the Bavarian State Government (No. 44-6521a/20/5). Further, we thank Allianz

Risk Consulting GmbH / Allianz Zentrum für Technik (AZT) for providing us with a large number of PV modules.

## References

- [1] Takuya Akiba, Shotaro Sano, Toshihiko Yanase, Takeru Ohta, and Masanori Koyama. Optuna: A next-generation hyperparameter optimization framework. In *Proceedings of the 25th ACM SIGKDD International Conference on Knowledge Discovery & Data Mining*, pages 2623–2631, 2019.
- [2] David Bernecker, Christian Riess, Elli Angelopoulou, and Joachim Hornegger. Continuous short-term irradiance forecasts using sky images. *Solar Energy*, 110:303–315, 2014.
- [3] C Buerhop, T Winkler, T Patel, J Hauch, C Camus, and CJ Brabec. Performance analysis of pre-cracked pv modules at cyclic loading conditions. In *35th EU PVSEC*, page 1554, 2018.
- [4] C. Buerhop, S. Wirsching, S. Gehre, T. Pickel, T. Winkler, A. Bemm, J. Mergheim, C. Camus, J. Hauch, and C. J. Brabec. Lifetime and degradation of pre-damaged pv-modules – field study and lab testing. In *2017 IEEE 44th Photovoltaic Specialist Conference (PVSC)*, pages 3500–3505, 2017.
- [5] Claudia Buerhop, Sven Wirsching, Andreas Bemm, Tobias Pickel, Philipp Hohmann, Monika Nieß, Christian Vodermayr, Alexander Huber, Bernhard Glück, Julia Mergheim, et al. Evolution of cell cracks in pv-modules under field and laboratory conditions. *Progress in Photovoltaics: Research and Applications*, 26(4):261–272, 2018.
- [6] C Buerhop-Lutz, T Winkler, FW Fecher, A Bemm, J Hauch, C Camus, and CJ Brabec. Performance analysis of pre-cracked pv-modules at realistic loading conditions. *Proceedings of the 33rd European PV-SEC, 5CO*, 8:1451–1456, 2017.
- [7] Claudia Buerhop-Lutz and Mathis Hoffmann. ELPVPower: A dataset for large scale PV power prediction using EL images, 2020.
- [8] Claudia Buerhop-Lutz, Mathis Hoffmann, Luca Reeb, Tobias Pickel, Jens Hauch, and Andreas Maier. Applying Deep Learning Algorithms to EL-images for Predicting the Module Power. In *Proceedings of the 36th European Photovoltaic Solar Energy Conference and Exhibition*, pages 858 – 863, 2019.
- [9] Sergiu Deitsch, Vincent Christlein, Stephan Berger, Claudia Buerhop-Lutz, Andreas Maier, Florian Gallwitz, and Christian Riess. Automatic classification of defective photovoltaic module cells in electroluminescence images. *Solar Energy*, 185:455–468, 2019.
- [10] Jia Deng, Wei Dong, Richard Socher, Li-Jia Li, Kai Li, and Li Fei-Fei. Imagenet: A large-scale hierarchical image database. In *2009 IEEE conference on computer vision and pattern recognition*, pages 248–255. Ieee, 2009.



- [11] Harris Drucker, Christopher JC Burges, Linda Kaufman, Alex J Smola, and Vladimir Vapnik. Support vector regression machines. In *Advances in neural information processing systems*, pages 155–161, 1997.
- [12] Rajiv Dubey, Shashwata Chattopadhyay, Sachin Zachariah, Sugguna Rambabu, K Hemant, Singh Anil Kottantharayil, Brij M Arora, KL Narasimhan, Narendra Shiradkar, and Juzer Vasi. On-site electroluminescence study of field-aged pv modules. In *2018 IEEE 7th World Conference on Photovoltaic Energy Conversion (WCPEC)(A Joint Conference of 45th IEEE PVSC, 28th PVSEC & 34th EU PVSEC)*, pages 0098–0102. IEEE, 2018.
- [13] F. Farress, A. El Hassani Alaoui, M.N. Saidi, A. Tamtaoui, Z. Zaimi, and A. Bennouna. Defect detection in solar cells using electroluminescence imaging and image processing algorithms. volume 8, 2017.
- [14] Andrew M. Gabor, Rob Janoch, Andrew Anselmo, and Halden Field. Solar panel design factors to reduce the impact of cracked cells and the tendency for crack propagation. In *2015 NREL PV Module Reliability Workshop*.
- [15] Andrew M Gabor, Rob Janoch, Andrew Anselmo, Jason L Lincoln, Hubert Seigneur, and Christian Honeker. Mechanical load testing of solar panels—beyond certification testing. In *2016 IEEE 43rd Photovoltaic Specialists Conference (PVSC)*, pages 3574–3579. IEEE, 2016.
- [16] Kaiming He, Xiangyu Zhang, Shaoqing Ren, and Jian Sun. Identity mappings in deep residual networks. In *European conference on computer vision*, pages 630–645. Springer, 2016.
- [17] Geoffrey E Hinton and Sam T Roweis. Stochastic neighbor embedding. In *Advances in neural information processing systems*, pages 857–864, 2003.
- [18] Mathis Hoffmann, Bernd Doll, Florian Talkenberg, Christoph J Brabec, Andreas K Maier, and Vincent Christlein. Fast and robust detection of solar modules in electroluminescence images. In *International Conference on Computer Analysis of Images and Patterns*, pages 519–531. Springer, 2019.
- [19] Bernd Jähne. *Digitale Bildverarbeitung*. Springer, 2013.
- [20] Sarah Kajari-Schröder, Iris Kunze, Ulrich Eitner, and Marc Köntges. Spatial and orientational distribution of cracks in crystalline photovoltaic modules generated by mechanical load tests. *Solar Energy Materials and Solar Cells*, 95(11):3054–3059, 2011.
- [21] Ahmad Maroof Karimi, Justin S Fada, Nicholas A Parrilla, Benjamin G Pierce, Mehmet Koyutürk, Roger H French, and Jennifer L Braid. Generalized and mechanistic pv module performance prediction from computer vision and machine learning on electroluminescence images. *IEEE Journal of Photovoltaics*, 10(3):878–887, 2020.

- [22] M Köntges, S Kajari-Schröder, I Kunze, and U Jahn. Crack statistic of crystalline silicon photovoltaic modules. In *26th EU PVSEC*, volume 26, pages 3290–3294, 2011.
- [23] Timo Kropp, Markus Schubert, and Jürgen H Werner. Quantitative prediction of power loss for damaged photovoltaic modules using electroluminescence. *Energies*, 11(5):1172, 2018.
- [24] Wei-Chen Li and Du-Ming Tsai. Wavelet-based defect detection in solar wafer images with inhomogeneous texture. *Pattern Recognition*, 45(2):742–756, 2012.
- [25] Martin Mayr, Mathis Hoffmann, Andreas Maier, and Vincent Christlein. Weakly supervised segmentation of cracks on solar cells using normalized l<sub>p</sub> norm. In *2019 IEEE International Conference on Image Processing (ICIP)*, pages 1885–1889. IEEE, 2019.
- [26] Maxime Oquab, Leon Bottou, Ivan Laptev, and Josef Sivic. Learning and transferring mid-level image representations using convolutional neural networks. In *Proceedings of the IEEE conference on computer vision and pattern recognition*, pages 1717–1724, 2014.
- [27] Maxime Oquab, Léon Bottou, Ivan Laptev, and Josef Sivic. Is object localization for free?-weakly-supervised learning with convolutional neural networks. In *Proceedings of the IEEE conference on computer vision and pattern recognition*, pages 685–694, 2015.
- [28] Eneko Ortega, Gerardo Aranguren, and Juan Carlos Jimeno. New monitoring method to characterize individual modules in large photovoltaic systems. *Solar Energy*, 193:906–914, 2019.
- [29] Nobuyuki Otsu. A threshold selection method from gray-level histograms. *IEEE transactions on systems, man, and cybernetics*, 9(1):62–66, 1979.
- [30] Marco Paggi, Mauro Corrado, and Irene Berardone. A global/local approach for the prediction of the electric response of cracked solar cells in photovoltaic modules under the action of mechanical loads. *Engineering Fracture Mechanics*, 168:40–57, 2016.
- [31] Adam Paszke, Sam Gross, Francisco Massa, Adam Lerer, James Bradbury, Gregory Chanan, Trevor Killeen, Zeming Lin, Natalia Gimelshein, Luca Antiga, et al. Pytorch: An imperative style, high-performance deep learning library. In *Advances in Neural Information Processing Systems*, pages 8024–8035, 2019.
- [32] Fabian Pedregosa, Gaël Varoquaux, Alexandre Gramfort, Vincent Michel, Bertrand Thirion, Olivier Grisel, Mathieu Blondel, Peter Prettenhofer, Ron Weiss, Vincent Dubourg, et al. Scikit-learn: Machine learning in python. *Journal of machine learning research*, 12(Oct):2825–2830, 2011.

- [33] M Sander, S Dietrich, M Pander, S Schweizer, M Ebert, and J Bagdahn. Investigations on crack development and crack growth in embedded solar cells. In *Reliability of Photovoltaic Cells, Modules, Components, and Systems IV*, volume 8112, page 811209. International Society for Optics and Photonics, 2011.
- [34] Mark Sandler, Andrew Howard, Menglong Zhu, Andrey Zhmoginov, and Liang-Chieh Chen. Mobilenetv2: Inverted residuals and linear bottlenecks. In *Proceedings of the IEEE conference on computer vision and pattern recognition*, pages 4510–4520, 2018.
- [35] Eric J Schneller, Rafaela Frota, Andrew M Gabor, Jason Lincoln, Hubert Seigneur, and Kristopher O Davis. Electroluminescence based metrics to assess the impact of cracks on photovoltaic module performance. In *2018 IEEE 7th World Conference on Photovoltaic Energy Conversion (WCPEC)(A Joint Conference of 45th IEEE PVSC, 28th PVSEC & 34th EU PVSEC)*, pages 0455–0458. IEEE, 2018.
- [36] Ali Sharif Razavian, Hossein Azizpour, Josephine Sullivan, and Stefan Carlsson. Cnn features off-the-shelf: an astounding baseline for recognition. In *Proceedings of the IEEE conference on computer vision and pattern recognition workshops*, pages 806–813, 2014.
- [37] Daniel Stromer, Andreas Vetter, Hasan Can Oezkan, Christian Probst, and Andreas Maier. Enhanced crack segmentation (ecs): A reference algorithm for segmenting cracks in multicrystalline silicon solar cells. *IEEE Journal of Photovoltaics*, 2019.
- [38] Janine Teubner, Claudia Buerhop, Tobias Pickel, Jens Hauch, Christian Camus, and Christoph J Brabec. Quantitative assessment of the power loss of silicon pv modules by ir thermography and its dependence on data-filtering criteria. *Progress in Photovoltaics: Research and Applications*, 27(10):856–868, 2019.
- [39] Jason Yosinski, Jeff Clune, Yoshua Bengio, and Hod Lipson. How transferable are features in deep neural networks? In *Advances in neural information processing systems*, pages 3320–3328, 2014.

# Appendices

## A Detection results

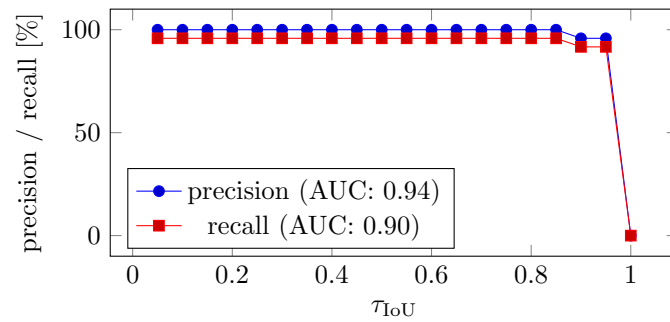


Figure 10: Detection performance of the proposed method. We compute the IoU of predicted and ground truth boxes. Then, we state a prediction as accepted, if the IoU with the ground truth box is greater than  $\tau_{IoU}$ . Finally, we compute precision and recall at varying thresholds  $\tau_{IoU}$ . It turns out that the method works very well up to  $\tau_{IoU} = 0.85$  and slightly drops in precision and recall beyond that threshold.

## B Additional CAMs

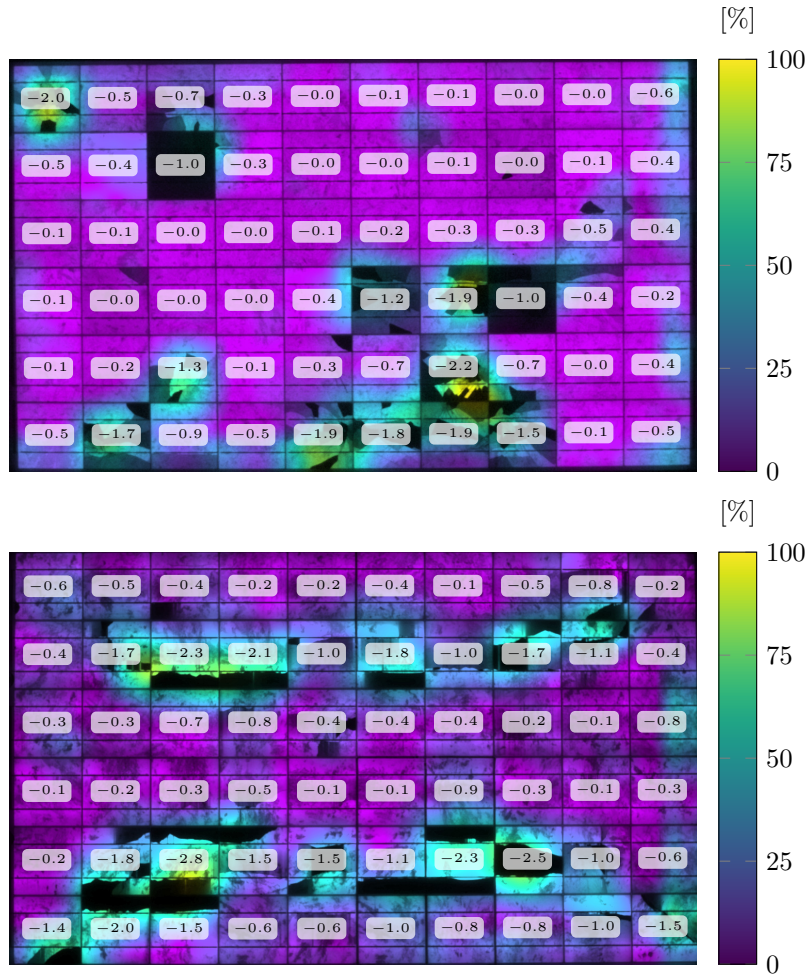


Figure 11: Additional examples for CAMs used to compute the per cell power loss.

## C Data analysis

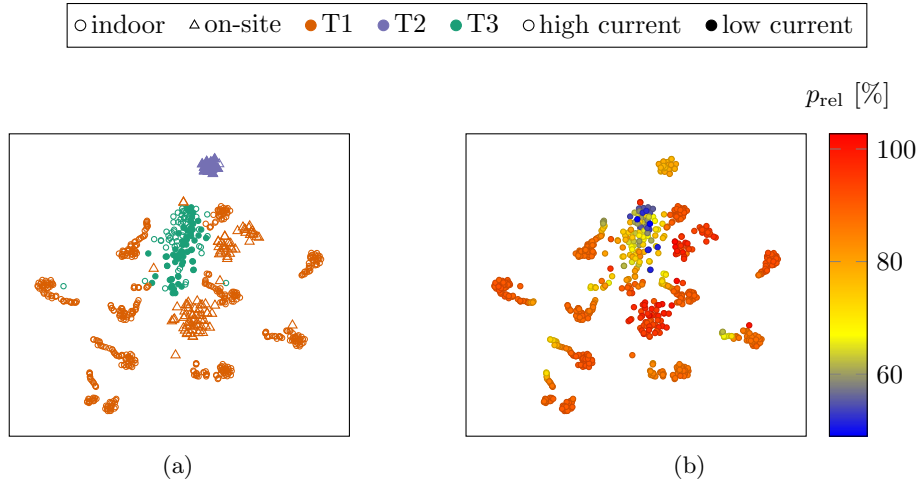


Figure 12: t-stochastic neighbour embedding (t-SNE) visualization of ResNet18 embeddings.

In Fig. 12, we visualize our data using t-stochastic neighbour embedding (t-SNE) [17] applied on the embeddings from a pretrained ResNet18. We observe that there is a weak clustering according to  $p_{\text{rel}}$  without any further training. This is in line with the results from an earlier publication on the same topic, where a pretrained ResNet18 already performed well on this task by only training the last fully connected layer [8]. In addition, Fig. 12 reveals that module instances from the load cycle measurements result in dense clusters. A further analysis of the data shows that there is a strong clustering regarding module types and measurement conditions in the t-SNE visualization, as shown in Appendix C. We conclude that  $p_{\text{rel}}$  is not the main mode of variation without further finetuning of the network. This observation is supported by the results obtained from using a pretrained ResNet18 followed by a SVR, which we introduce as a baseline method (Sec. 5.2).